International Journal of
MATERIALS RESEARCH

Zeitschrift für METALLKUNDE

Original Contributions

Martin Vlach[a], Jakub Cizek[a], Bohumil Smola[a], Ivana Stulikova[a], Petr Hruska[a], Veronika Kodetova[a], Stanislav Danis[a], Dhritti Tanprayoon[b], Volkmar Neubert[c]

[a] Charles University, Faculty of Mathematics and Physics, Prague, Czech Republic
[b] National Metal and Materials Technology Center (MTEC), National Science and Technology Development Agency (NSTDA), Pathum Thani, Thailand
[c] Institut für Materialprüfung und Werkstofftechnik, Clausthal-Zellerfeld, Germany

Influence of dislocations on precipitation processes in hot-extruded Al–Mn–Sc–Zr alloy

Solute clustering and precipitation processes in hot-extruded Al–Mn–Sc–Zr alloy were studied. Positron annihilation studies were combined with electrical resistometry, microhardness testing and microstructural characterization. Extrusion introduced dislocations which arranged into a cell structure. Sc solutes segregated at dislocations. Moreover, fine coherent $Al_3(Sc,Zr)$ particles precipitated during extrusion and subsequent cooling. During the isochronal annealing Sc agglomerated forming Sc-rich dispersoids. Agglomeration of Sc solutes is facilitated by pipe diffusion along dislocations. Zr atoms become mobile above 240 °C and form shells surrounding Al_3Sc particles. This process is not affected by dislocations. The maximum fraction of positrons annihilated by Sc and Zr electrons occurred at 300 °C, coinciding with hardening of the alloy. The resistivity changes above 300 °C are caused by precipitation of Mn-containing particles.

Keywords: Hot deformation; $Al_3(Sc,Zr)$ precipitates; Solute clustering; Positron annihilation spectroscopy; Electron microscopy

1. Introduction

Microstructures and recrystallization of Al-based alloys are significantly influenced by the small additions of Sc ($\sim$ 0.2 at.%) and Zr ($\sim$ 0.1 at.%) [1–7]. These alloys are promising materials for high-temperature structural applications [1, 2, 6]. The favorable properties are related to the formation of a dense and homogeneous distribution of coherent $Al_3(Sc,Zr)$ precipitates with $L1_2$ structure [1–10]. The complex nanostructure of the $Al_3(Sc,Zr)$ phase has been discussed in several recent articles by studies using conventional and high-resolution transmission electron microscopy or atom-probe tomography [5, 7–11]. It has been shown that Sc-rich clusters in as-cast Al–Sc–Zr alloys can be formed in the early stages of precipitation at temperatures above $\sim$200 °C [8, 11, 12]. These clusters subsequently transform into Al_3Sc particles with the $L1_2$ structure. When Zr diffusion becomes significant, dispersoids with a complex core–shell structure consisting of an Al_3Sc core embedded in an $Al_3(Sc,Zr)$ shell are developed [8, 11, 12]. The authors of the present study have already provided resistivity and positron annihilation measurements of the Al–Sc–Zr-based alloy which showed that Zr-segregation at the Al_3Sc/α-Al matrix interfaces might take place already at $\sim$270 °C [12, 13].

Manganese is the most widely used transition metal in commercial aluminum alloys [1, 2]. Thus an effect of Mn-containing particles, which were introduced during heat treatment, on properties of Al–Mn-based alloys has been studied extensively, e.g. Refs. [5, 8, 10, 14]. Precipitation of these particles in Al influences resistivity behavior significantly, although it has an insignificant effect on microhardness [8, 10, 12].

The aim of the present work was to study the early phase transformation stages of the hot-extruded Al–Mn–Sc–Zr alloys during isochronal annealing. Plastic hot deformation in the course of extrusion at increased temperatures can lead to the precipitation of Sc(,Zr)-containing particles and can introduce dislocations which might affect solute clustering and precipitation processes. To examine these effects precipitation processes in hot-extruded Al–Mn–Sc–Zr alloy were compared with those in conventionally cast alloy studied in Ref. [12]. The results of measurements of electrical resistivity, microhardness and microstructure investigations were combined. Positron annihilation spectroscopy (PAS) enabling characterization of defects and investigation of clustering of solute atoms at the atomic scale was used as well. Two complementary PAS techniques were employed in the present work: (i) positron lifetime (LT) spectroscopy [15] which enables identification of open volume defects in the sample and (ii) coincidence Doppler broadening (CDB) [16] which carries information about a local chemical environment of defects. CDB is a unique technique for investigation of early stages of precipitation and has been successfully employed for studies of this phenomenon [17, 18].

2. Experimental procedure

The chemical composition of the hot-extruded Al–Mn–Sc–Zr alloy was determined as: 0.68 at.% Mn, 0.15 at.% Sc, 0.05 at.% Zr, ≤0.01 at.% the other elements and Al balance. The alloy was conventionally prepared by melting of pure Al and master alloys (Al-10Mn, Al-2Sc and Al-10Zr) in a resistance furnace at ∼850 °C. The alloy was cast into a cylindrical steel mold with 7 cm diameter and then extruded at ∼350 °C in one step with a cross-section reduction 70 : 18. Hot extrusion ensures decrease of porosity that might be introduced during casting. The measured density of the hot-extruded alloy ((2 710 ± 30) kg · m^{-3}) is close to the theoretical density (2 730 kg · m^{-3}) indicating very low porosity.

The isochronal annealing from room temperature (RT) up to 390 °C was performed in steps 30 K/30 min in the same way as in Refs. [8, 10, 12]. The samples were annealed in an oil bath (up to 240 °C) or in a furnace with argon protective atmosphere (270 – 390 °C). Each annealing step was finished by quenching into liquid nitrogen or water, respectively, in order to preserve the microstructure developed during the annealing.

Electrical resistometry measurements were performed at 78 K in a liquid N_2 bath. The electrical resistance was measured by means of the dc four-point method with a dummy specimen in series (used for correction of temperature instability of the liquid N_2 bath) within a relative accuracy of ∼10^{-4}. The effect of parasitic thermo-electromotive forces was suppressed by changing the current polarity. H-shaped specimens machined to dimensions of 2 mm × 9 mm × 90 mm were used for these measurements; the length represents the gauge length. The deformation of electrical field in the vicinity of contacts was estimated yielding measured resistance accuracy better than ∼1 %. The accuracy of specimen dimension measurement is about 2 %, which is also the accuracy of the absolute resistivity values [19]. The major contribution to the temperature independent resistivity component in the alloys comes from solutes in the matrix. Contributions of dislocations or of subgrain and grain boundaries in Al–Mn- and Al–Sc–Zr-based alloys are two orders of magnitude lower [13, 20 – 22].

The positron source utilized in LT and CDB measurements was made of as a small drop of ^{22}Na chloride with activity of 1 MBq deposited and dried between 2 μm thick Mylar C covering foils. The LT measurements were carried out using a digital spectrometer [23] equipped with BaF_2 scintillators and Hamamatsu H3378 photomultipliers and exhibiting a time resolution of 145 ps. Typically, 10^7 coincidence events were accumulated in each LT spectrum. The LT spectra were decomposed into exponential components by means of a maximum-likelihood procedure [24]. The source contribution was determined using a well-annealed high-purity Al specimen and consists of two components. The component with a lifetime of ∼368 ps and relative intensity of ∼7 % represents a contribution of positrons annihilated in the ^{22}NaCl source spot. The long-lived component with a lifetime of ∼1.5 ns and intensity of ∼1 % comes from pick-off annihilation of ortho-positronium formed in the covering Mylar foils.

The CDB investigations were performed using a digital spectrometer [25] equipped with two high purity Ge detectors and characterized by energy resolution of 0.9 keV at 511 keV. The two dimensional CDB energy spectra were reduced into one-dimensional cuts representing the Doppler broadened (DB) annihilation profiles. In this paper the DB profiles are presented as the ratio curves related to the well annealed pure Al reference specimen.

The influence of isochronal annealing (steps of 30 K/30 min) on mechanical properties was studied using Vickers microhardness (HV0.5) testing performed at RT using a load of 0.5 kg and a loading time of 10 s.

Transmission electron microscopy (TEM) with BRUKER energy-dispersive X-ray microanalysis and electron diffraction (ED) was carried out in a JEOL JEM 2000FX electron microscope. The structure of the alloys was also determined by metallographic microscope Jena Metaval 85618 and scanning electron microscope (SEM) MIRA I Schottky FE-SEMH equipped with BRUKER X-ray microanalyser. Specimens were prepared by polishing in "Flick Etch Solution" (1.3 vol.% HCl and 0.87 vol.% HF solution in distilled water). X-ray diffraction (XRD) was performed in Bragg–Brentano geometry on a Bruker D8 Advance diffractometer equipped with Cu X-ray tube.

3. Results

3.1. Hot-extruded state of the Al–Mn–Sc–Zr alloy

The as-prepared state of the Al–Mn–Sc–Zr alloy exhibits a two-component LT spectrum: the shorter component with lifetime $\tau_1 = (90 \pm 3)$ ps and relative intensity $I_1 = (14 \pm 1)$ % comes from free positrons (not trapped at defects), while the longer component with the lifetime $\tau_2 = (233 \pm 1)$ ps and intensity $I_2 = (86 \pm 1)$ % represents a contribution of positrons trapped at defects. A fine grain structure (0.5 – 2.0 μm) was observed by TEM (see Fig. 1a) in the alloy in the cross section of the extrusion direction. Figure 1a also shows dislocations in relatively high density forming a cellular structure with cell size 100 – 300 nm in grain interiors. This structure is hardly visible in grains oriented out of

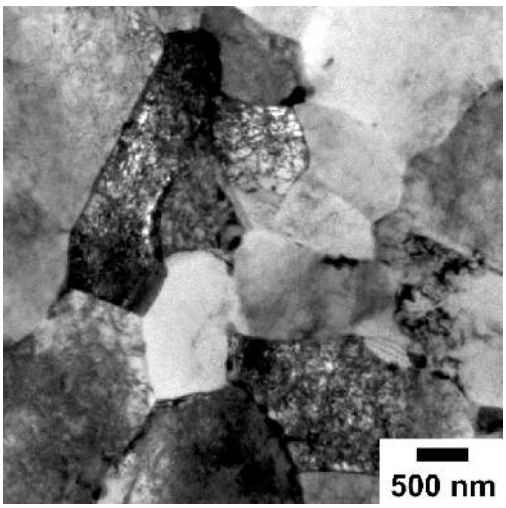

(a)

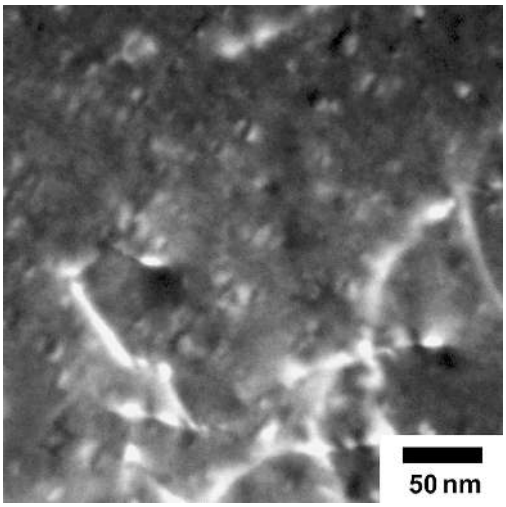

(b)

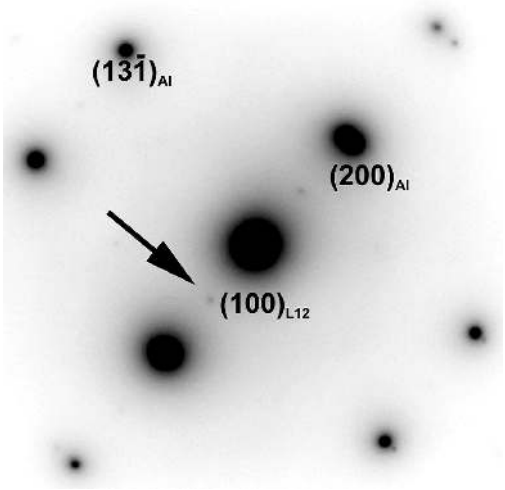

(c)

Fig. 1. (a) TEM bright field image of the dislocation arrangement and grain structure, (b) dark field weak beam TEM image of fine coherent Al_3Sc and/or $Al_3(Sc,Zr)$ particles in coffee-bean contrast, (c) [013] α-Al matrix zone ED pattern with diffraction spots of the Al_3Sc and/or $Al_3(Sc,Zr)$ particles (arrow).

strong dynamic contrast. Cell walls are mostly constituted by individual dislocations. Dislocations are tangled only in a minority of walls; see white lines in Fig. 1b. Precipitation of the fine coherent Al_3Sc and/or $Al_3(Sc,Zr)$ particles ($L1_2$, cP4 structure) with size of (5 ± 2) nm predominantly situated in grain interiors was also revealed (Fig. 1b). The ED pattern of the $L1_2$-structured particles in the alloy is shown in Fig. 1c. No precipitates other than Al_3Sc and/or $Al_3(Sc,Zr)$ were observed by TEM, which means that Mn-containing phase (if any) has very low volume fraction.

Since the lifetime τ_2 agrees well with the value reported for dislocations in Al [26, 27], the component with lifetime τ_2 can be attributed to positrons trapped at dislocations. It is generally accepted that dislocations are only shallow traps incapable of complete positron confinement [28, 29]. Positrons weakly localized in the dislocation core are spread along the dislocation line and become finally trapped at vacancies anchored in the compressive elastic field of the dislocation [30]. Hence, final positron traps are vacancy-like defects, namely vacancies "squeezed" by the compressive elastic field of dislocation [26, 30]. The mean dislocation density in the sample can be calculated using a suitable positron trapping model. TEM observations revealed that grains in the hot-extruded sample consist of dislocation-free cells separated by walls comprising either single dislocations or tangled dislocations, as shown in Fig. 1b. Hence, the spatial distribution of dislocations is non-uniform since dislocations are located mainly in the dislocation walls. Non-uniform spatial distribution of dislocations in the hot-extruded sample is also indicated by the LT results. The quantity $\tau_f = (I_1/\tau_1 + I_2/\tau_2)^{-1}$ [15] calculated from LT data is (189 ± 4) ps. This value is significantly higher than the bulk positron lifetime for Al τ_B = 161 – 164 ps [26, 31]. Such behavior is typical for non-uniform distribution of dislocations in deformed metals [32 – 34]. The density of dislocations in the as-prepared sample can be determined using the diffusion positron trapping model (DTM) developed for metals with cellular dislocation structure [32, 33, 35].

Within DTM it is assumed that the sample consists of spherical cells with radius R and negligible density of dislocations. Cells are separated by dislocation walls with thickness δ containing a high density of dislocations $\rho_{D,wall}$. Based on TEM observations (Fig. 1b) we estimated $\delta \sim$ 10 nm. The mean dislocation density is:

$$\rho_D = \eta \rho_{D,wall} \tag{1}$$

where

$$\eta = \frac{(2R)^3}{(2R+\delta)^3} \tag{2}$$

is the volume fraction of dislocation walls.

Positrons stopped inside dislocation walls are quickly trapped at dislocations while positrons stopped inside the cell interiors may by annihilated either in the free state and/or may reach dislocation walls by diffusion and be trapped at dislocations there. This is taken into account in DTM by solution of the positron diffusion-annihilation equation [32]:

$$\frac{\partial n_f}{\partial t} = D_+ \left(\frac{\partial^2 n_f}{\partial r^2} + \frac{2}{r} \frac{\partial n_f}{\partial r} \right) - \tau_B^{-1} n_f \tag{3}$$

where D_+ is the positron diffusion coefficient [36] and n_f is the probability that a positron is alive in the free state at time t and distance r from the center of the cell. Equation (3) is solved with the boundary condition

$$\left(\frac{\partial n_f}{\partial t}\right)_{r=R} = -\frac{v_D \rho_{D,wall} \delta}{D_+} n_f(R,t) \tag{4}$$

which expresses that the positron current passing through the interface between a cell and adjacent dislocation wall is proportional to the dislocation density $\rho_{D,wall}$ inside the wall.

The initial condition

$$n_f(r,0) = \frac{3}{4\pi}\frac{1-\eta}{R^3} \tag{5}$$

expresses that a positron stopped inside cell interior is in the free state at $t = 0$, while a positron stopped inside the dislocation wall is immediately trapped at a dislocation.

The probability N_f that a positron is alive in the free state at time t anywhere inside the cell is given by spatial integration of Eq. (5):

$$N_f(t) = 4\pi \int_0^R n_f(r,t) r^2 \mathrm{d}r \tag{6}$$

The probability N_D that a positron is at time t alive in the trapped state at a dislocation is governed by the rate equation

$$\frac{\mathrm{d}N_D(t)}{\mathrm{d}t} = -\tau_D^{-1} N_D(t) + 4\pi R^2 \delta v_D \rho_{D,wall} n_f(R,t) \tag{7}$$

where v_D is the specific positron trapping rate for dislocations and τ_D denotes the lifetime of positrons trapped at dislocations, here $\tau_D = \tau_2 \approx 233$ ps.

The positron lifetime spectrum is the negative derivative of solutions of Eqs. (6) and (7):

$$S(t) = -\frac{\mathrm{d}}{\mathrm{d}t}[N_f(t) + N_D(t)] \tag{8}$$

It can be written as a sum of infinite number of exponential components

$$S(t) = \sum_{i=1}^{\infty} \frac{I_{1,i}}{\tau_{1,i}} e^{-\frac{t}{\tau_{1,i}}} + \frac{I_2}{\tau_D} e^{-\frac{t}{\tau_D}} \tag{9}$$

with lifetimes

$$\tau_{1,i} = \left(\tau_B^{-1} + \frac{\beta_i^2 D_+}{R^2}\right)^{-1} \tag{10}$$

The coefficients β_i are roots of the equation

$$\beta_i \cot \beta_i + \alpha - 1 = 0 \tag{11}$$

where

$$\alpha = \frac{v_D \rho_{D,wall} \delta R}{D_+} \tag{12}$$

The relative intensities of the exponential components are

$$I_{1,i} = 3(1-\eta)\frac{v_D \rho_{D,wall} \delta}{R} a_i \left(\frac{1}{\tau_i^{-1} - \tau_B^{-1}} - \frac{1}{\tau_i^{-1} - \tau_D^{-1}}\right) \tag{13}$$

and

$$I_2 = \eta + 3(1-\eta)\frac{v_D \rho_{D,wall} \delta}{R} \sum_{i=1}^{\infty} \frac{a_i}{\tau_i^{-1} - \tau_D^{-1}} \tag{14}$$

where the coefficients a_i are

$$a_i = \frac{2\alpha}{\beta_i^2 + \alpha(\alpha - 1)} \tag{15}$$

The infinite sums in the above equations converge relatively fast to zero. Therefore, truncation of the summation at $i > \alpha$ is always acceptable [32]. Fitting of positron lifetime spectra by the model function (Eq. (9)) convoluted with the resolution function of the spectrometer enables determination of the mean cell size $2R$, i. e. the size of dislocation-free regions, and the mean dislocation density ρ_D.

Employing DTM and using the specific trapping rate for dislocations in Al $v_D = 0.5 \times 10^{-4}$ m^2 s^{-1} [37], the mean dislocation density of $(1.2 \pm 2) \times 10^{14}$ m^{-2} was determined for the sample. The cell size estimated by DTM is $2R = (240 \pm 30)$ nm. This value is consistent with the average size of cells (100 – 300 nm), i. e. dislocation-free regions inside grains observed by TEM in Fig. 1a. Note that some positrons can be trapped at vacancy-like misfit defects at grain boundaries having an open volume comparable with that of vacancies squeezed by the compressive elastic field of dislocations. Positrons trapped at grain boundaries also contribute, therefore, to the component with lifetime τ_2. Hence, grain boundaries are treated within DTM in the same manner as dislocation cells [32, 34].

The CDB ratio curve (related to well-annealed Al) for the hot-extruded alloy is plotted in Fig. 2a. The main feature of this curve is a peak located at $p \sim 9 \times 10^{-3}\ m_0 c$. The high momentum part of a CDB ratio curve can be expressed as a superposition of ratio curves for pure elements [18]. The ratio curve $\rho\ (p)$ for Al–Mn–Sc–Zr alloy can be expressed as [12]:

$$\begin{aligned}\rho(p) &= F_f \xi_{Al,f} + \xi_{Sc,f}\rho_{Sc,f}(p) + \xi_{Zr,f}\rho_{Zr,f}(p) \\ &+ \xi_{Mn,f}\rho_{Mn,f}(p) + F_D \xi_{Al,D}\rho_{Al,D}(p) + \xi_{Sc,D}\rho_{Sc,D}(p) \\ &+ \xi_{Zr,D}\rho_{Zr,D}(p) + \xi_{Mn,D}\rho_{Mn,D}(p)\end{aligned} \tag{16}$$

The curves $\rho_{x,f}(p)$ and $\rho_{x,D}(p)$, respectively, are ratio curves for free positrons and positrons trapped in vacancy-like defects annihilated by electrons belonging to the element x = Al, Sc, Zr, Mn. These curves were determined in Ref. [12]. The coefficients $\xi_{x,f}$ denote the probability that a free positron is annihilated by Al, Sc, Zr or Mn electron. Similarly the coefficients $\xi_{x,D}$ stand for the probabilities that the trapped positrons are annihilated by an Al, Sc, Zr or Mn electrons. These probabilities fulfill the normalization condition $\xi_{Al,f} + \xi_{Sc,f} + \xi_{Zr,f} + \xi_{Mn,f} = 1$ and $\xi_{Al,D} + \xi_{Sc,D} + \xi_{Zr,D} + \xi_{Mn,D} = 1$. The symbols F_f and F_D denote the fraction of positrons annihilated in the free and the trapped

state, respectively, and they are normalized so that $F_f + F_D = 1$.

If alloying elements are completely dissolved in Al matrix, the coefficients $\xi_{x,f}$ equal to their atomic concentration in the alloy, i.e. $\xi_{Sc,f} = 1.5 \times 10^{-3}$, $\xi_{Zr,f} = 5 \times 10^{-4}$ and $\xi_{Mn,f} = 6.8 \times 10^{-3}$. These values are so low that the probability that a free positron will be annihilated by Sc, Zr or Mn electron can be considered as negligible. Thus, a detectable contribution of annihilation by Sc, Zr or Mn electrons can appear only from trapped positrons if there is a segregation of solutes at defects, i.e. the local chemical environment of defects is enriched in a particular solute. Taking this into account Eq. (16) can be simplified into the form:

$$\rho(p) = (1 - F_D) + F_D\left[\xi_{Al,D}\rho_{Al,D}(p) + \xi_{Sc,D}\rho_{Sc,D}(p) + \xi_{Zr,D}\rho_{Zr,D}(p) + \xi_{Mn,D}\rho_{Mn,D}(p)\right] \quad (17)$$

Solute segregation at defects (here dislocations) indeed occurs in the hot-extruded alloy since the ratio curve $\rho(p)$ in Fig. 2a significantly differs from unity. Comparison of the ratio curve $\rho(p)$ with the ratio curves $\rho_{x,D}(p)$ for various elements plotted in Fig. 2b revealed that a peak at $p \sim 9 \times 10^{-3}$ m_0c can be caused by the contribution of positrons annihilated with Sc and/or Zr electrons.

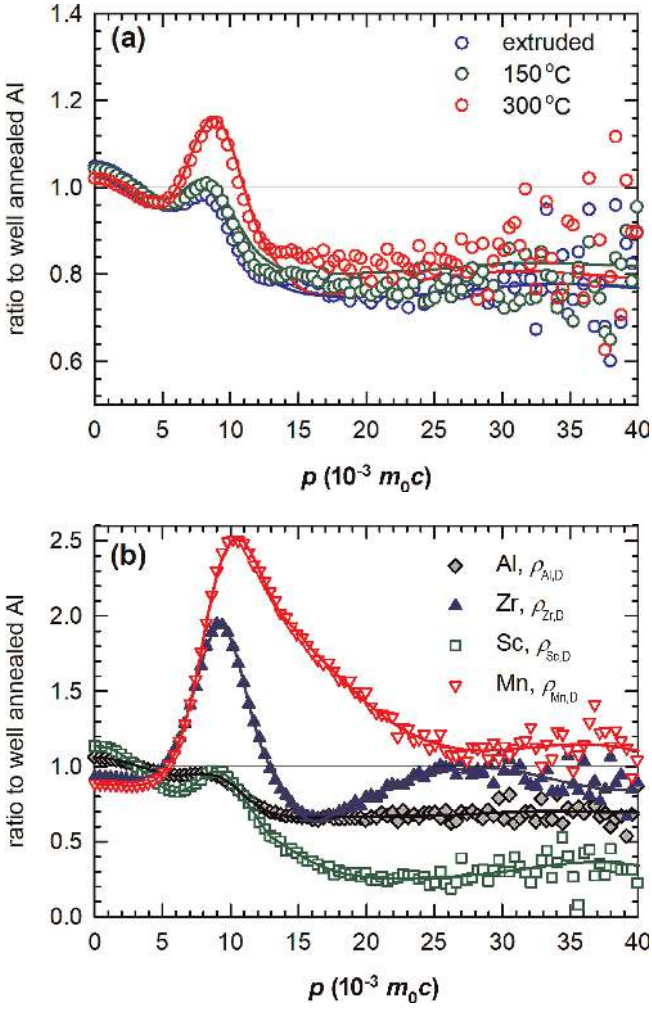

Fig. 2. CDB ratio curves for (a) the alloy in the hot-extruded state and selected annealed states (up to 150 °C and 300 °C), and (b) heavily cold-rolled high purity Al, Sc, Zr and Mn reference samples.

The ratio curve $\rho(p)$ for the hot-extruded alloy was fitted by superposition of the curves $\rho_{x,D}(p)$ using the fraction of F_D of positrons trapped at defects estimated from the LT data [38]:

$$F_D = I_2 \frac{\tau_2 - \tau_B}{\tau_2 - I_2\tau_B} \quad (18)$$

The superposition of the ratio curves $\rho_{x,D}(p)$ is plotted in Fig. 2a by a solid line. The coefficients $\xi_{Al,D} = 0.30 \pm 0.05$, $\xi_{Sc,D} = 0.65 \pm 0.05$, $\xi_{Zr,D} = 0.05 \pm 0.02$, $\xi_{Mn,D} = 0$ were obtained from fitting for the hot-extruded sample. Hence, a substantial portion of trapped positrons in the hot-extruded alloy is annihilated by Sc electrons. This corresponds to a significant segregation of Sc solutes at dislocations during hot extrusion. There is also a minor contribution of trapped positrons annihilated by Zr electrons while the contribution of positrons annihilated by Mn electrons can be considered as negligible. It has been shown that defect-free Sc(,Zr)-containing particles cannot confine positrons [39] but positron trapping may occur at vacancy-like defects located either inside the particles or at their interfaces with the Al matrix. Dislocations in the hot-extruded sample probably provide nucleation centers for the Al_3Sc and/or $Al_3(Sc,Zr)$ particles. As a consequence positrons trapped at dislocations annihilate with higher probability in the vicinity of the Al_3Sc and/or $Al_3(Sc,Zr)$ particles.

3.2. Development of hot-extruded Al–Mn–Sc–Zr alloy during isochronal annealing

3.2.1. Positron annihilation spectroscopy

The mean positron lifetime is a robust parameter not influenced by correlations of fitting parameters [15]. The development of the mean positron lifetime with annealing temperature is plotted in the inset in Fig. 3a. In general, the mean positron lifetime decreases with temperature indicating certain recovery of defects. Overall decrease of the mean positron lifetime is interrupted by local maxima at ~240 and ~320 °C which can be attributed to precipitation effects. More information can be obtained from the decomposition of positron lifetime spectra. The lifetime spectra of the alloy studied are well described by two components at all annealing temperatures. The development of the lifetimes τ_1, τ_2 of these components with increasing annealing temperature during isochronal annealing is plotted in Fig. 3a. The lifetime τ_2 remains approximately constant during the annealing. This indicates that the nature of positron traps, i.e. vacancy-like defects, remains unchanged. The intensity I_2 of positrons trapped at defects is shown in Fig. 3b. In general I_2 slightly decreases with annealing temperature indicating a certain decrease in the concentration of defects, most probably a slight reduction in the dislocation density. This overall behavior is postponed in the temperature range 120–180 °C (labeled stage I) and 200–270 °C (labeled stage II). Finally the behavior of I_2 is reversed above 290 °C and I_2 increases with temperature (stage III). As will be shown in the following text these stages of I_2 development are connected with precipitation effects.

Figure 4 shows the development of CDB ratio curves with increasing annealing temperature (the CDB ratio curves for selected annealed states (150 °C and 300 °C) are plotted in Fig. 2a). One can see that the peak at $p \approx 9 \times 10^{-3}\ m_0c$ representing a contribution of trapped positrons annihilated by Sc and/or Zr electrons increases with temperature and exhibits a local maximum at ∼180 °C. Further annealing above 240 °C led to an even more pronounced increase of this contribution with a maximum at ∼300 °C. These changes are caused by precipitation of Sc(,Zr)-rich particles. To obtain quantitative information about the Sc(,Zr)-rich phase precipitation the ratio curves measured at various temperatures were fitted by Eq. (17). We obtained from fitting that $\xi_{Mn,d}$ equals zero at all annealing temperatures up to 390 °C. The fractions $\xi_{Sc,d}$ and $\xi_{Zr,d}$ obtained from fitting are plotted in Fig. 5a as a function of annealing temperature. Figure 5b shows temperature dependence of the fraction F_D of positrons trapped at defects as calculated from LT data using Eq. (18). The majority of trapped positrons in the hot-extruded sample are annihilated by Sc electrons due to segregation of Sc at dislocations. It can be seen in Fig. 5a that the fraction of positrons annihilated by Sc electrons $\xi_{Sc,D}$ firstly decreases

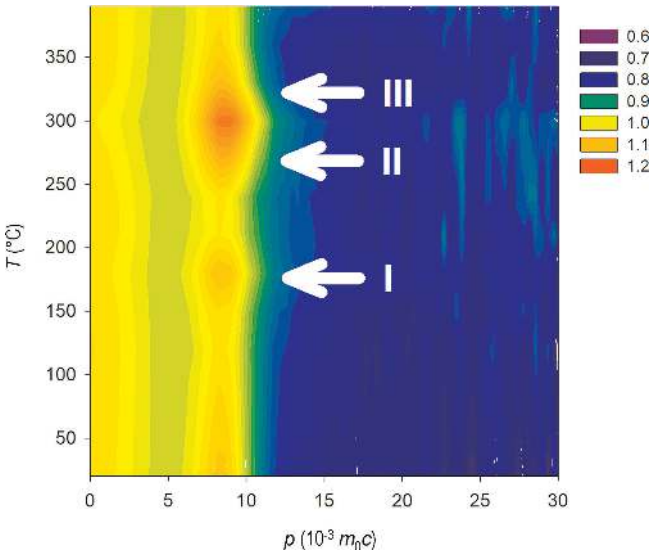

Fig. 4. The development of CDB ratio curves for the hot-extruded Al–Mn–Sc–Zr alloy with increasing annealing temperature. Color coded *z*-axis is the ratio with respect to a well-annealed Al reference.

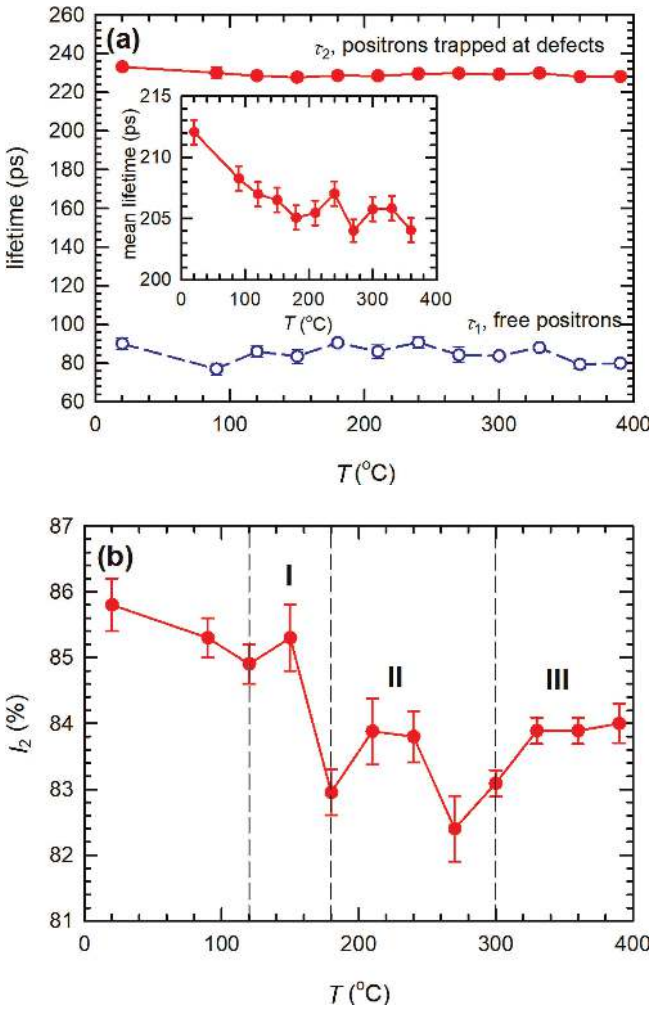

Fig. 3. (a) Temperature dependence of lifetimes of components resolved in LT spectra, and (b) the intensity I_2 of positrons trapped at defects for the hot-extruded Al–Mn–Sc–Zr alloy.

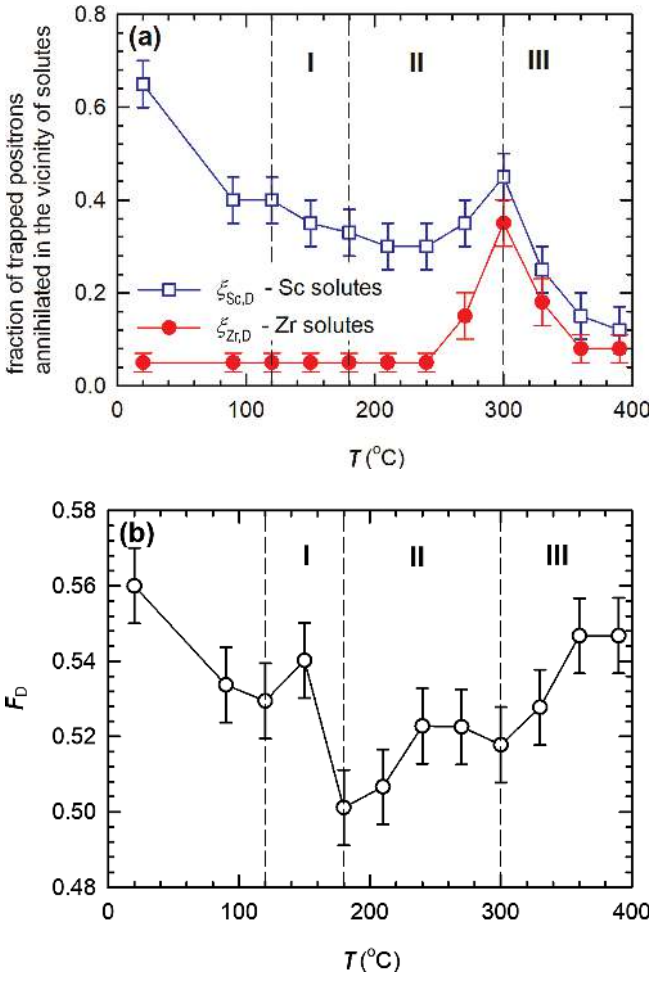

Fig. 5. Temperature dependence of fractions: (a) $\xi_{Sc,d}$ and $\xi_{Zr,d}$ of positrons trapped at defects and annihilated by Sc and Zr electrons, respectively, obtained by fitting of CDB ratio curves; (b) F_D of positrons trapped at defects calculated from LT results by Eq. (3).

with annealing temperature. This is caused by agglomeration of Sc atoms into small clusters which subsequently develop into the Al_3Sc particles. Since Sc solutes are located predominantly around dislocations Sc-rich clusters nucleate at dislocations. Agglomeration makes the distribution of Sc atoms along dislocations inhomogeneous. The distance between Sc-rich clusters is obviously larger than the average distance between Sc solutes when they are randomly distributed along dislocations as individual atoms. As a consequence $\xi_{Sc,D}$ decreases and more trapped positrons are annihilated by Al electrons. This is accompanied by a slight decrease in the dislocation density detected by LT spectroscopy and demonstrated by a decrease in I_2 in Fig. 3b and F_D in Fig. 5b. However formation of Sc clusters introduced new positron traps since Sc-rich dispersoids contain vacancies, especially in the early stages of their precipitation [40, 41]. This is reflected by weak local maxima of I_2 and F_D in the temperature range corresponding to stage I. Vacancies mediate agglomeration of Sc solutes to clusters. Hence one can conclude that stage I is caused by clustering of Sc solutes. In cast AlMnScZr alloy the clustering of solutes started at $\sim 150\,^{\circ}C$ [12]. The onset of Sc clustering is shifted to lower temperatures ($\Delta \sim 30\,^{\circ}C$) in this hot-extruded alloy containing a high density of dislocations since diffusivity of Sc solutes is enhanced by diffusion along dislocations. Migration of Zr solutes starts above $240\,^{\circ}C$ and a Zr shell is built around the Al_3Sc particles [12]. Hence, stage II can be attributed to formation of the Sc,Zr-containing particles with a complex core–shell structure. Both fractions of positrons annihilated by Sc and by Zr electrons increase in stage II, see Fig. 5a. Stage II is not influenced by dislocations and occurs in the comparable temperature range as in cast Al-0.70 at.%Mn-0.15 at.%Sc-0.047 at.%Zr alloy where no second-phase particles in the as-prepared state were observed [12].

3.2.2. Electrical resistivity and microhardness testing

Electrical resistivity and microhardness isochronal annealing curves from RT up to $390\,^{\circ}C$ are shown in Fig. 6a. No resistivity changes were observed up to $210\,^{\circ}C$. Then resistivity decreases to a minimum after annealing up to $390\,^{\circ}C$. The HV0.5 curve exhibits a weak age hardening peak at $\sim 300\,^{\circ}C$. This hardening peak corresponds well to stage II and is, therefore, caused by formation of the $Al_3(Sc,Zr)$ particles with a complex core–shell structure. The negative numerical derivative (spectrum curve) of the electrical resistivity annealing curve is plotted in Fig. 6b. The spectrum curve exhibits weak changes with a maximum at $\sim 290\,^{\circ}C$ (i.e. within stage II). Distinctive changes of resistivity start at temperatures above $\sim 300\,^{\circ}C$, i.e. in stage III (see Fig. 6b). It can also be seen that the precipitation process above $300\,^{\circ}C$ does not lead to hardening.

4. Discussion

Combining PAS, electrical resistivity and microhardness data one can conclude that there are three processes taking place during isochronal annealing of the hot-extruded Al–Mn–Sc–Zr alloy.

(i) Clustering of Sc solutes occurs in the temperature range $120-210\,^{\circ}C$ (stage I). This process is facilitated by dislocations and occurs at lower temperatures in the studied alloy than in the cast material studied in Ref. [12]. In the early stages of precipitation Sc enriched dispersoids exhibit imperfect structure and contain vacancy-like defects [40, 41]. Further annealing leads to development of these dispersoids into Al_3Sc particles with Ll_2 structure. It has to be mentioned that the extruded alloy contains the Al_3Sc and/or $Al_3(Sc,Zr)$ particles already in the hot-extruded state in contrast to the as-cast alloy (see Ref. [12]) where no such particles were found. These Al_3Sc and/or $Al_3(Sc,Zr)$ particles were formed in the course of hot extrusion and do not take part in the precipitation processes during isochronal annealing minimally up to $210\,^{\circ}C$. But precipitation of the Al_3Sc and/or $Al_3(Sc,Zr)$ phase during hot extrusion reduced the concentration of Sc dissolved in matrix. Hence, although the hot-extruded sample still contains dissolved Sc its concentration in the matrix is significantly lower than in the cast material [12] and Sc solutes are located preferentially along dislocations. As a consequence clustering of Sc solutes during isochronal annealing is facilitated by pipe diffusion along dislocation lines. Significantly lower concentration of Sc dissolved in matrix in the as-extruded sam-

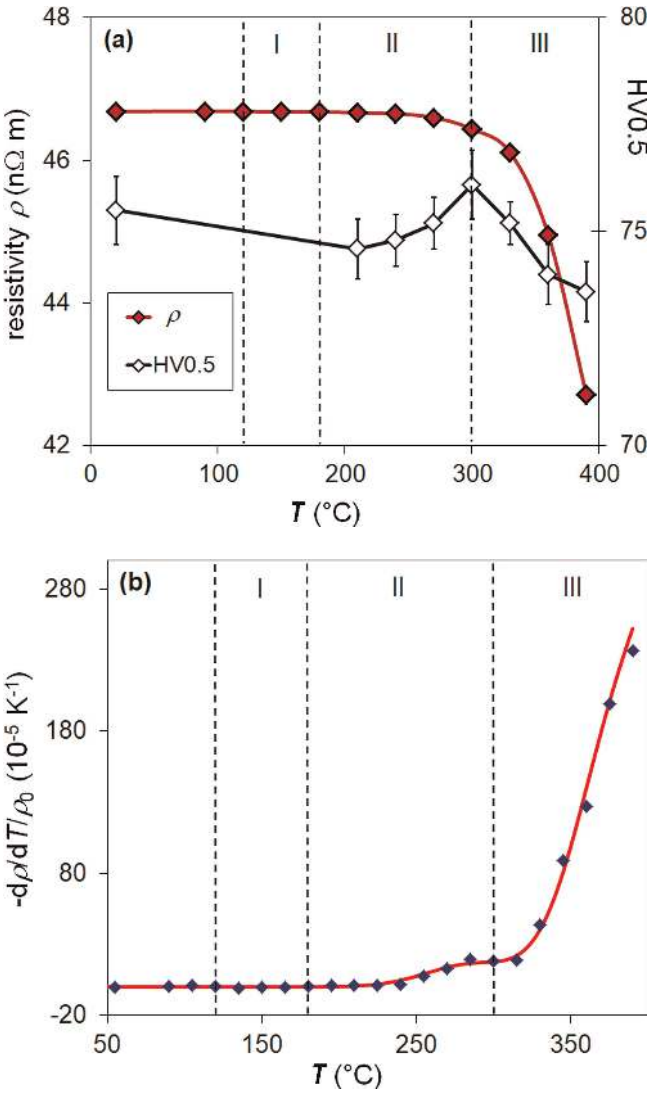

Fig. 6. (a) Annealing curve of electrical resistivity and HV0.5 microhardness, (b) electrical resistivity spectrum constructed from resistivity data in the panel (a).

ple compared to the as-cast material is also indicated by absence of a stage corresponding to clustering of Sc solutes in the electrical resistivity curve of the extruded sample while for the cast material such a stage was clearly observed at ~200 °C [12]. Hence, the clustering of Sc solutes in the hot-extruded sample was observed only by PAS (as stage I) since it occurs in the vicinity of dislocations which trap positrons.

(ii) Zr solutes are incorporated into Al_3Sc particles forming $Al_3(Sc,Zr)$ particles with a complex core–shell structure in the temperature range 240–300 °C (within stage II). It can be seen from the CDB measurements that no Zr-response to annealing was observed up to ~240 °C. This is in accordance with a lower diffusivity of Zr in the Al matrix [42, 43] as well as with our previous study in the as-cast AlMnScZr alloy where Zr atoms were found to segregate at ~270 °C [12]. Figure 5a shows that annealing above 240 °C is connected not only with an increase of $\xi_{Sc,D}$ but also with a rise in $\xi_{Zr,D}$. Microstructural observation of hot-deformed AlMnScZr alloy in our previous study (see Ref. [8]) proved a coarsening of the particles with the $L1_2$-structure during subsequent annealing up to 330 °C. These results indicate that stage II can be ascribed to the additional Al_3Sc-phase formation and formation of Zr-enriched shell of these dispersoids. It agrees well with previous studies of cast Al–Mn–Sc–Zr alloy where the Al_3Sc-phase particles also precipitate (at ~270 °C) and Zr solutes segregate at Al_3Sc/α-Al matrix interfaces (at ~280 °C) [11, 12]. Hence, contrary to clustering of Sc solutes, the formation of the $Al_3(Sc,Zr)$ particles with a complex core–shell structure is almost unaffected by dislocations. This can be easily understood. Kinetics of Sc clustering is limited by diffusivity of Sc solutes while development of the $Al_3(Sc,Zr)$ particles with a core–shell structure is limited by diffusivity of Zr atoms. Sc solutes segregate at dislocations and their diffusivity is, therefore, enhanced by pipe diffusion along dislocations. On the other hand, Zr solutes exhibit only a weak tendency to segregation at dislocations [12, 13]. As a consequence the influence of dislocations on Zr solute diffusivity is insignificant in the studied alloy. Note that investigations of hot-deformed AlMnScZr alloy [8] revealed that dislocation density in the alloy heated with the same effective heating rate as in the present work (1 K/1 min) remains practically unchanged up to ~340 °C.

(iii) At temperatures above 300 °C the diffusivity of Mn solutes becomes significant and Mn-containing dispersoids can be formed [8, 10, 14, 44–46]. Hence stage III can be attributed to agglomeration of Mn solutes and formation of Mn-rich dispersoids. The positron affinity for both Mn and Zr is lower in absolute value than that for the Al matrix [47]. Hence, defect-free coherent Mn and Zr particles are not attractive for positrons [39]. Since formation of Mn-containing dispersoids led to an increase in I_2 (see Fig. 3b) as well as F_D (Fig. 5b) these dispersoids must contain vacancy-like misfit defects at the interfaces with the matrix. Positrons trapped at these vacancy-like defects contribute to the component with lifetime τ_2. Mn atoms have smaller atomic radii than Zr ones and tend to be located in central parts of dispersoids where positron density is low while larger Zr atoms segregate at interfaces containing vacancy-like defects. As a consequence, formation of Mn-containing dispersoids leads to an increase of I_2 but Mn contribution to CDB spectra is insignificant, see Fig. 2a. Note that similar behavior was observed in Al–Sc–Mg [48] and Al–Sc–Ti alloys [49] where Mg and Ti atoms with larger radii segregate at dispersoid interfaces while smaller Sc atoms are pushed into centers. Taking into account the Sc- and Zr-behavior at comparable temperatures [10, 12, 43, 50, 51] and the known contribution of the Mn-, Sc- and Zr-concentration to the resistivity of Al (e. g. [1, 22, 45]) the resistivity development in the alloy at annealing temperatures above ~300 °C is mainly associated with the change in the Mn concentration in the Al matrix. Moreover, our previous study on the hot-deformed AlMnScZr alloy (see Ref. [8, 10]) proved the precipitation of Al_6Mn particles at grain boundaries at ~300 °C and inside grains at ~340 °C. The microstructure of the studied alloy annealed up to 390 °C with mostly Mn,Fe-containing particles determined from XRD peaks (see Fig. 7) can be ascribed to the C-base centered orthorhombic phase Al_6Mn or to its modifications ($Al_{12}Mn_3Fe_3$, $Al_6(Mn,Fe)$ and $Al_6(Mn,Fe,Si)$) with lattice parameters $a = 0.75$ nm, $b = 0.65$ nm and $c = 0.88$ nm [5, 8, 45, 46]. TEM performed on the alloy treated up to 420 °C confirms the presence of the Al_6Mn and/or $Al_6(Mn,Fe)$ particles at (sub)grain boundaries (see Ref. [8]). Figure 6 shows that precipitation of the Mn-containing particles in the studied alloy has no hardening effect.

5. Conclusions

The results of positron lifetime spectroscopy, coincidence Doppler broadening, electrical resistometry, microhardness measurements and microstructure investigations of the hot-extruded Al–Mn–Sc–Zr alloy can be summarized as follows:

1. The hot-extruded alloy contains a high density of dislocations arranged into a cell structure. The average cell size was determined as (240 ± 30) nm. Segregation of Sc solutes at dislocations was detected. Moreover, fine coherent Al_3Sc and/or $Al_3(Sc,Zr)$ particles precipitated during hot extrusion at 350 °C.

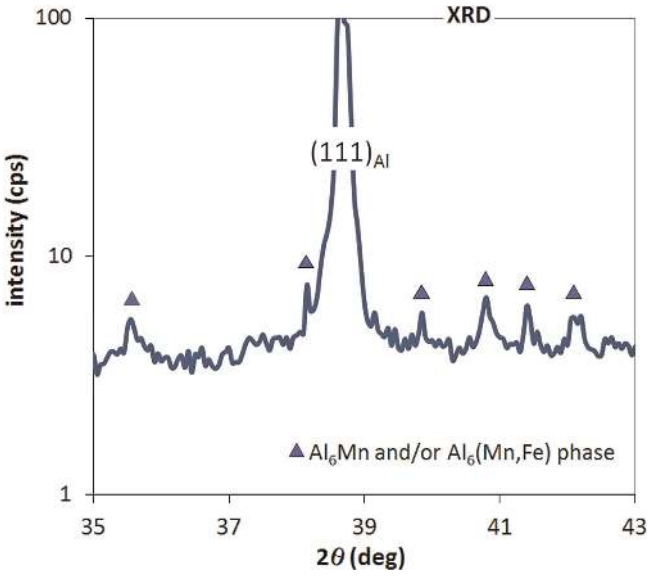

Fig. 7. Detail of XRD patterns for hot-extruded Al–Mn–Sc–Zr alloy after annealing up to 390 °C.

2. Clustering of Sc solutes takes place during isochronal annealing of the alloy in the temperature range 120–210 °C. This process is enhanced by pipe diffusion of Sc solutes along dislocations. Sc-rich dispersoids further develop into particles with $L1_2$ structure.
3. Zr solute migration starts above ~240 °C contributing to the development of Sc,Zr-containing particles with $L1_2$ structure. This process is limited by diffusivity of Zr solutes and is almost unaffected by dislocations. The maximum of positrons annihilated by Sc and Zr electrons occurred at ~300 °C, coinciding with the peak hardness of the alloy.
4. The resistivity decreases and fraction of positrons in the trapped state increases after annealing at temperatures higher than 300 °C. This is mainly caused by precipitation of Mn-containing particles. Nevertheless, the precipitation has a negligible effect on microhardness.

This work was supported by The Czech Science Foundation (GACR), projects 16-12828S and 17-17139S, and by the Grant Agency of Charles University, project 324015.

References

[1] L.S. Toropova, D.G. Eskin, M.L. Kharakterova, T.V. Dobatkina: Advanced Aluminium Alloys Containing Scandium – Structure and Properties, Gordon and Breach Science Publisher, The Netherlands (1998).
[2] J. Røyset, R. Ryum: Int. Mater. Rev. 50 (2005) 19. DOI:10.1179/174328005X14311
[3] Z. Jia, J. Røyset, J.K. Solberg, Q. Liu: Trans. Nonferrous Met. Soc. China 22 (2012) 1866. DOI:10.1016/S1003-6326(11)61399-X
[4] R. Guan, Y. Shen, Z. Zhao, X. Wang: J. Mater. Sci. Technol. 33 (2017) 215. DOI:10.1016/j.jmst.2017.01.017
[5] M. Vlach, I. Stulíkova, B. Smola, H. Cisarova, J. Piesova, S. Danis, R. Gemma, J. Malek, D. Tanprayoon, V. Neubert, Int. J. Mater. Res 103 (2012) 814. DOI:10.3139/146.110712
[6] J.H. Li, B. Oberdorfer, S. Wurster, P. Schumacher: J. Mater. Sci. 49 (2014) 5961. DOI:10.1007/s10853-014-8315-z
[7] N.Q. Vo, D.C. Dunand, D.N. Seidman: Acta Mater. 63 (2014) 73. DOI:10.1016/j.actamat.2013.10.008
[8] M. Vlach, I. Stulikova, B. Smola, T. Kekule, H. Kudrnova, V. Kodetova, V. Ocenasek, J. Malek, V. Neubert: Kovove Materialy-Metallic Materials 53 (2015) 295. DOI:10.4149/km_2015_5_295
[9] L. Lityńska, J. Dutkiewicz, K. Parliński: Z. Metallkd. 97 (2006) 321. DOI:10.3139/146.101258
[10] M. Vlach, I. Stulikova, B. Smola, T. Kekule, H. Kudrnova, S. Danis, R. Gemma, V. Ocenasek, J. Malek, D. Tanprayoon, V. Neubert: Mater. Charact. 86 (2013) 59. DOI:10.1016/j.matchar.2013.09.010
[11] W. Lefebvre, F. Danoix, H. Hallem, B. Forbord, A. Bostel, K. Marthinsen: J. Alloys Compd. 470 (2009) 107. DOI:10.1016/j.jallcom.2008.02.043
[12] M. Vlach, J. Čížek, O. Melikhova, I. Stulíková, B. Smola, T. Kekule, H. Kudrnová, R. Gemma, V. Neubert: Metall. Mater. Trans. A 46 (2015) 1556. DOI:10.1007/s11661-015-2767-x
[13] M. Vlach, I. Stulíková, B. Smola, N. Žaludová, J. Černá: J. Alloys Compd. 492 (2010) 143. DOI:10.1016/j.jallcom.2009.11.126
[14] F.G. Coury, C.S. Kiminami, W.J. Botta, C. Bolfarini, M.J. Kaufman: Materials & Design 110 (2016) 436. DOI:10.1016/j.matdes.2016.08.008
[15] P. Hautojärvi, C. Corbel, in: A. Dupasquier, A.P. Mills (Eds.), Positron spectroscopy of solids, Proceedings of the International School of Physics "Enrico Fermi", IOS Press, Amsterdam, The Netherlands (1995) 491. DOI:10.3254/978-1-61499-211-0-491
[16] P. Asoka-Kumar, M. Alatalo, V.J. Ghosh, A.C. Kruseman, B. Nielsen, K.G. Lynn: Phys. Rev. Lett. 77 (1996) 2097. PMid:10061856; DOI:10.1103/PhysRevLett.77.2097
[17] S.M. He, N.H. van Dijk, H. Schut, E.R. Peekstok, S. van der Zwaag: Phys. Rev. B 81 (2010), no. 094103. DOI:10.1103/PhysRevB.81.094103
[18] A. Somoza, M.P. Petkov, K.G. Lynn, A. Dupasquier: Phys. Rev. B 65 (2002), no. 094107. DOI:10.1103/PhysRevB.65.094107
[19] M. Hájek, J. Veselý, M. Cieslar: Mater. Sci. Eng. A 462 (2007) 339. DOI:10.1016/j.msea.2006.01.175
[20] A. von Bassewitz, E.N. Mitchell: Phys. Rev. 182 (1969) 712. DOI:10.1103/PhysRev.182.712
[21] Y. Ueda, H. Tamura, E. Hashimoto: J. Phys.-Condens. Mater 6 (1994) L637. DOI:10.1088/0953-8984/6/43/001
[22] F.R. Fickett: Cryogenics 11 (1971) 349. DOI:10.1016/0011-2275(71)90036-1
[23] F. Bečvář, J. Čížek, I. Procházka, J. Janotová: Nucl. Inst. Meth. in Phys. Research A 539 (2005) 372. DOI:10.1016/j.nima.2004.09.031
[24] I. Prochazka, I. Novotny, F. Becvar: Mater. Sci. Forum 255–257 (1997) 772. DOI:10.4028/www.scientific.net/MSF.255-257.772
[25] J. Čížek, M. Vlček, I. Procházka: Nucl. Inst. Meth. in Phys. Research A 623 (2010) 982. DOI:10.1016/j.nima.2010.07.046
[26] J. Čížek, I. Procházka, T. Kmječ, P. Vostrý: Phys. Stat. Sol. A 180 (2000) 439. DOI:10.1002/1521-396X(200008)180:2<439::AID-PSSA439>3.0.CO;2-9
[27] H. Murakami, T. Endo, I. Matsuda: Phys. Rev. B 44 (1991), no. 2504. DOI:10.1103/PhysRevB.44.2504
[28] Y. Kamimura, T. Tsutsumi, E. Kuramoto: Phys. Rev. B 52 (1995), no. 879. DOI:10.1103/PhysRevB.52.879
[29] K. Sato, T. Yoshiie, T. Ishizaki, Q. Xu: Phys. Rev. B 75 (2007), no. 094109. DOI:10.1103/PhysRevB.75.094109
[30] L.C. Smedskjaer, M. Manninen, M.J. Fluss: J. Phys. F: Metal Physics 10 (1980), no. 2237. DOI:10.1088/0305-4608/10/10/019
[31] Y. Park, J.T. Waber, M. Meshii, C.L. Snead, C.G. Park: Phys. Rev. B 34 (1986), no. 823. DOI:10.1103/PhysRevB.34.823
[32] A. Dupasquier, R. Romero, A. Somoza: Phys. Rev. B 48 (1993), no. 9235. DOI:10.1103/PhysRevB.48.9235
[33] J. Čížek, I. Procházka, M. Cieslar, R. Kužel, J. Kuriplach, F. Chmelík, I. Stulíková, F. Bečvář, O. Melikhova: Phys. Rev. B 65 (2002), no. 094106. DOI:10.1103/PhysRevB.65.094106
[34] J. Čížek, M. Neslušan, M. Čilliková, A. Mičietová, O. Melikhova: J. Phys. D: Appl. Phys. 47 (2014), no. 445301. DOI:10.1088/0022-3727/47/44/445301
[35] B. Oberdorfer, R. Würschum: Phys. Rev. B 79 (2009), no. 184103. DOI:10.1103/PhysRevB.79.184103
[36] P.J. Schultz, K.G. Lynn, Rev. Mod. Phys. 60 (1988) 701. DOI:10.1103/RevModPhys.60.701
[37] G. Dlubek: Mater. Sci. Forum 13–14 (1987) 11. DOI:10.4028/www.scientific.net/MSF.13–14.11
[38] R.N. West, in: P. Hautojärvi (Ed.), Positrons in Solids, Positron Studies of Lattice Defects in Metals, Springer-Verlag, Berlin, Germany (1979) 89. DOI:10.1007/978-3-642-81316-0_3
[39] M. Vlach, J. Čížek, B. Smola, O. Melikhova, M. Vlček, V. Kodetová, H. Kudrnová, P. Hruška: Mater. Charact. 129 (2017) 1. DOI:10.1016/j.matchar.2017.04.017
[40] C. Booth-Morrison, D.C. Dunand, D.N. Seidman, Acta Mater. 59 (2011) 7029. DOI:10.1016/j.actamat.2011.07.057
[41] W.W. Zhou, B. Cai, W.J. Li, Z.X. Liu, S. Yang, Mater. Sci. Eng. A 552 (2012) 353. DOI:10.1016/j.msea.2012.05.051
[42] K.E. Knipling, D.C. Dunand, D.N. Seidman: Int. J. Mater. Res. 97 (2006) 246. DOI:10.3139/146.101249
[43] E. Clouet, A. Barbu: Acta Mater. 55 (2007) 391. DOI:10.1016/j.actamat.2006.08.021
[44] N.J. Luiggi: Metall. Mater. Trans. B 28 (1997) 149. DOI:10.1007/s11663-997-0137-9
[45] D. Vojtěch, K. Saksl, J. Verner, B. Bártová: Mater. Sci. Eng. A 428 (2006) 188. DOI:10.1016/j.msea.2006.05.017
[46] Y. Birol: J. Alloys Compd. 471 (2009) 122. DOI:10.1016/j.jallcom.2008.04.005

[47] M.J. Puska, P. Lanki, R.M. Nieminen, J. Phys.: Condens. Matter 1 (1989) 6081. DOI:10.1088/0953-8984/3/20/007
[48] E.A. Marquis, D.N. Seidman, M. Asta, C. Woodward, Acta Mater. 54 (2006) 119. DOI:10.1016/j.actamat.2005.08.035
[49] M. E. van Dalen, D.C. Dunand, D.N. Seidman, Acta Mater. 53 (2005) 4225. DOI:10.1016/j.actamat.2005.05.022
[50] S.I. Fujikawa, M. Sugaya, H. Takei, K.-I. Hirano: J. Less-Common Met. 63 (1979) 87. DOI:10.1016/0022-5088(79)90211-X
[51] Y.-B. Kang, A.D. Pelton, P. Chartrand, C.D. Fuerst: Calphad 32 (2008) 413. DOI:10.1016/j.calphad.2008.03.002

(Received August 23, 2017; accepted February 27, 2018; online since June 11, 2018)

Correspondence address

Dr. Martin Vlach
Faculty of Mathematics and Physics
Charles University
Ke Karlovu 3
Prague 2, 121 16
Czech Republic
Tel.: +420221911459
Fax: +420221911618
E-mail: martin.vlach@mff.cuni.cz
Web: www.mff.cuni.cz

Bibliography
DOI 10.3139/146.111654
Int. J. Mater. Res. (formerly Z. Metallkd.)
109 (2018) 7; page 583 – 592

ISSN 1862-5282